J. Mech. Phys. Solids Vol. 39, No. 7, pp. 963–986, 1991.
Printed in Great Britain.

0022-5096/91 $3.00 + 0.00

DUCTILE FAILURE OF A CONSTRAINED METAL FOIL

A. G. VARIAS, Z. SUO† and C. F. SHIH‡

Division of Engineering, Brown University, Providence, RI 02912, U.S.A.
†Department of Mechanical and Environmental Engineering, University of California, Santa Barbara, CA 93106, U.S.A.

(*Received* 30 *April* 1990)

ABSTRACT

A METAL foil bonded between stiff ceramic blocks may fail in a variety of ways, including de-adhesion of interfaces, cracking in the ceramics and ductile rupture of the metal. If the interface bond is strong enough to allow the foil to undergo substantial plastic deformation dimples are usually present on fracture surfaces and the nominal fracture energy is enhanced. Ductile fracture mechanisms responsible for such morphology include (i) growth of near-tip voids nucleated at second-phase particles and or interface pores, (ii) cavitation and (iii) interfacial debonding at the site of maximum stress which develops at distances of several foil thicknesses ahead of the crack tip. For a crack in a low to moderately hardening bulk metal, it is known that the maximum mean stress which develops at a distance of several crack openings ahead of the tip does not exceed about three times the yield stress. In contrast, the maximum mean stress that develops at several foil thicknesses ahead of the crack tip in a constrained metal foil can increase continuously with the applied load. Mean stress and interfacial traction of about four to six times the yield of the metal foil can trigger cavitation and/or interfacial debonding. The mechanical fields which bear on the competition between failure mechanisms are obtained by a large deformation finite element analysis. Effort is made to formulate predictive criteria indicating, for a given material system, which one of the several mechanisms operates and the relevant parameters that govern the nominal fracture work. The shielding of the crack tip in the context of ductile adhesive joints, due to the non-proportional deformation in a region of the order of the foil thickness, is also discussed.

1. INTRODUCTION

AMONG the materials being considered for high-performance power propulsion systems are ceramics and intermetallics containing controlled amounts of ductile metals. An example is high ceramic content composites made by infiltrating molten metal into a ceramic preform containing pore channels. Laminates with alternate ceramic and metal sheets, and ceramic components diffusion or liquid state bonded with metal foils are other examples. When these composites are loaded, the plastic deformation in metals is constrained by the surrounding elastic solids and high mean stress usually develops. Metals constrained as such exhibit failure modes that are not normally observed in unconstrained deformation. In a tensile test of a lead wire bonded in a glass cylinder, for instance, ASHBY *et al.* (1989) observed that the wire failed by the unstable growth of a single cavity. This behavior is intriguing, because, under unconstrained tension, the same lead wire failed by drawing to a point. The unusual

‡Author to whom correspondence should be addressed.

instability of the constrained lead wire has been rationalized on the basis of high triaxiality induced cavitation by HUANG *et al.* (1990). Specifically, a cavity in an infinite elastic–plastic solid is shown to grow unstably at a critical triaxiality (the ratio of the mean stress to the uniaxial yield strength, σ_m/σ_0). The critical triaxiality for non-hardening metals is about 4, and such a high level is rarely attained in common metal deformation modes. For example, an isolated plane strain crack in a non-hardening metal induces a maximum triaxiality of about 2.4 (RICE and JOHNSON, 1970).

A sequence of experiments has been recently conducted with ceramic plates sandwiching metal foils (DALGLEISH *et al.*, 1983; DALGLEISH *et al.*, 1989; REIMANIS *et al.*, 1990; REIMANIS and EVANS, 1991). Plasticity effects on the overall mechanical properties such as nominal strength and fracture energy are explored. When interfacial adhesion is strong and the foil is thin, an array of cavities is observed to nucleate and grow at distances several foil thicknesses ahead of the crack tip (Fig. 1). The length scale of the above failure mode is different from that for a crack in a bulk metal where voids nucleate and grow ahead of the crack tip within distances of the order of crack tip opening. As a consequence the nucleated cavities do not coalesce with the crack tip. Instead with further loading new cavities are nucleated at even larger distances from the crack tip leading to a rising crack growth resistance curve. The bridging zone develops until the cavities nearest to the tip coalesce with the crack.

In this paper the fields that develop in a constrained metal foil are obtained by a full-field large deformation elastic–plastic finite element analysis. These detailed fields are necessary for understanding the different failure modes that have been observed in experiments. We formulate predictive criteria indicating, for a given material system, whether high triaxiality induced cavitation and/or interfacial de-adhesion will be favored over near-tip void coalescence, and how these failure mechanisms govern the nominal fracture energy.

2. A LARGE DEFORMATION ELASTIC–PLASTIC ANALYSIS

2.1. *Material specification*

The competition of the various failure modes can be studied by a systematic analysis of the boundary value problem shown in Fig. 1. A metal foil of thickness h is bounded between two identical elastic substrates. Young's moduli and Poisson's ratios are E and ν for the metal foil and E_s and ν_s for the substrates. The plastic deformation of the metal is governed by a finite strain J_2 flow theory which is discussed in Appendix A. Strain hardening is controlled by a hardening function $H(\bar{\varepsilon}^p)$ which evolves according to the isotropic relation

$$H(\bar{\varepsilon}^p) = \sigma_0\left(1+\frac{\bar{\varepsilon}^p}{\varepsilon_0}\right)^{1/n}, \tag{1}$$

where n is the strain hardening exponent, $\bar{\varepsilon}^p$ the equivalent plastic strain, σ_0 the initial yield stress and ε_0 the reference strain ($\varepsilon_0 = \sigma_0/E$). Our implementation is based on a visco-plastic relation; however, the strain rate sensitivity m is assigned a value of

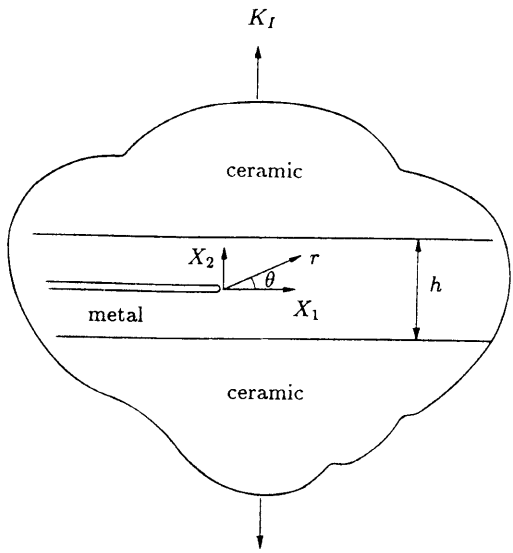

FIG. 1. A metal foil bonded between two ceramic substrates, with a centerline crack. The elastic K_I-field is applied at distance $r \gg h$.

0.005 which is appropriate for metals exhibiting essentially rate-independent behavior. Thus our analysis pertains to a rate-independent material with initial yield stress σ_0 and hardening exponent n.

Most of the results presented are for a ceramic/metal with properties

$$E/\sigma_0 = 300, \quad n = 10, \quad \nu = 0.33, \quad \nu_s = 0.2, \quad E_s/E = 5. \tag{2}$$

Nevertheless, the overall features of the fields can be regarded as generic and the trends apply to other material combinations as well. In the interest of space, the detailed fields for the other material combinations that we investigated are not presented. Quantities which are important to the interpretation of failure competition and the computation of the nominal fracture toughness are tabulated.

2.2. *Boundary value problem*

A crack lies along the centerline of the foil of thickness h. The foil is thin compared to the overall specimen dimension, so that plane strain deformation prevails and at distances large compared to h the stress field in the substrates can be represented by the homogeneous mode I elastic crack-tip field

$$\sigma_{ij}(r, \theta) \sim \frac{K_I}{\sqrt{(2\pi r)}} f_{ij}(\theta), \quad r \gg h, \tag{3}$$

where the angular functions f_{ij} can be found in fracture mechanics textbooks. The remote mode I stress intensity factor, K_I, can be related to the actual applied load via elasticity calibration appropriate for the given specimen.

The nominal energy-release rate, G, is given by Irwin's formula

$$G = \frac{1-\nu_s^2}{E_s} K_I^2. \tag{4}$$

The elastic constants in Eq. (4) are those of the substrate material since the remote field is unaffected by the thin foil.

The boundary value problem has two independent length scales, h and $(K_I/\sigma_0)^2$. The latter length is of the order of the plastic zone size r_p, which is defined as the maximum radial distance of the contour line $\bar{\varepsilon}^p = 0.001$ from the crack tip. For vanishingly small plastic zones, $r_p \ll h$, an inner K-annulus of characteristic size r_K exists near the tip, the domain ranging $r_p < r_K \ll h$. Under this condition, the amplitude of the inner K-field, designated by K, is related to the remote K_I by

$$K = \left[\frac{E}{E_s}\left(\frac{1-\nu_s^2}{1-\nu^2}\right)\right]^{1/2} K_I. \tag{5}$$

The above relation follows directly by application of the path-independent J-integral (RICE, 1968). The plastic zone size relative to the layer thickness is given by $(K_I/(\sigma_0\sqrt{h}))^2$. In reporting our results, the non-dimensional load parameter $K_I/(\sigma_0\sqrt{h})$ is used.

3. ELEVATION OF STRESS TRIAXIALITY

Within the limits of small-scale yielding defined by $r_p \ll h$, the fields in the region $r < r_K$ are self-similar, i.e., the stresses have the form $\sigma_{ij} = \sigma_0 g_{ij}(r/(K/\sigma_0)^2, \theta)$. For a modest increase of applied load beyond that of small-scale yielding, the crack-tip fields in the metal foil are again self-similar but are of the form $\sigma_{ij} = \sigma_0 h_{ij}(r/(J_{nf}/\sigma_0), \theta)$. Here J_{nf} is the value of the J-integral evaluated within the near-field annulus $5\delta_t < r < r_p$, where δ_t is the crack tip opening displacement. Self-similar fields for a plane strain crack in a bulk homogeneous material have been discussed by RICE and JOHNSON (1970) and MCMEEKING (1977).

3.1. *Evolution of high stresses*

Our analysis of the boundary value problem, using the mesh depicted in Fig. 10 of Appendix A, shows that the fields are nearly self-similar for plastic zone size less than $h/4$; for larger plastic zones the stresses deviate from the self-similar distribution, the difference becoming significant when r_p is greater than h. The above trends can be seen by examining the behavior of the mean stress σ_m, defined by $\sigma_m = (\sigma_{11}+\sigma_{22}+\sigma_{33})/3$. Figure 2 shows the triaxiality distribution along $X_2 = 0$ for four load levels as parameterized by $K_I/(\sigma_0\sqrt{h})$. The distance from the tip is normalized by J_{nf}/σ_0; J_{nf} is the value of the J-integral evaluated from the near-fields within the annulus $5\delta_t < r < r_p$ using the domain integral formulation (LI *et al.*, 1985). Since $J_{nf}/\sigma_0 \approx 2\delta_t$, the abscissa ranges from 0 to about $16\delta_t$. The finite strain zone is of order $3\delta_t$—therefore the distances examined in Fig. 2 do span length scales of relevance. The

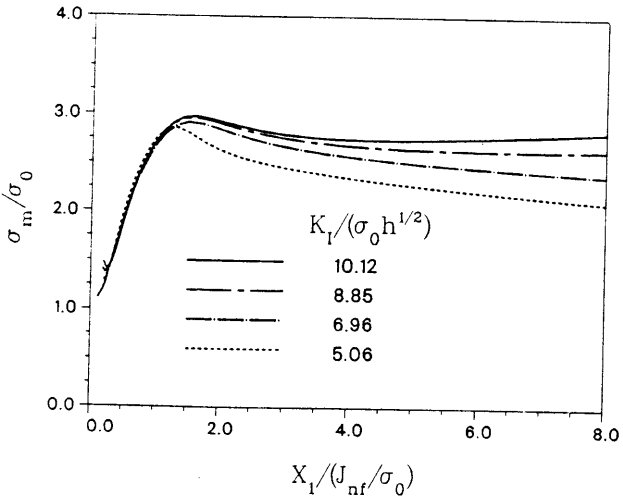

FIG. 2. Distribution of near tip triaxiality for various loading levels. J_{nf} is the near-field path-independent value of the J-integral. The triaxiality increases continuously with applied load.

stress triaxiality reaches a maximum of about 3 at $X_1 \approx 3\delta_t$, which is just beyond the zone of finite strains. It can also be seen that the mean stress levels increase with the applied load. These trends are representative of the behavior of the other stress components. In passing we note that the mean stress distribution for the smallest applied load, $K_I/(\sigma_0\sqrt{h}) = 5.06$, corresponds to a σ_{22} distribution which is nearly identical to that given by MCMEEKING (1977).

When r_p exceeds $3h$, the character of the mean stress distribution is changed. At $K_I/(\sigma_0\sqrt{h}) = 10.1$ ($r_p = 3.3h$), a second triaxiality maximum of 3.4 develops at a distance $1.1h$ ahead of the crack tip. The second maximum, denoted by σ_m^*, increases almost linearly with the applied load. Moreover its location, X_1^*, shifts farther ahead of the tip with increasing load. Displayed in Fig. 3a is the triaxiality distribution along the centerline of the metal foil for four load levels. For loads beyond $K_I/(\sigma_0\sqrt{h}) = 12.7$ ($r_p > 4.7h$), the near-tip triaxiality maximum vanishes altogether and the near-tip stress level decreases. In contrast, the stresses at $r > h$ and the larger stress maximum increase rapidly with the applied load. These same fields are replotted against distance normalized by $(K_I/\sigma_0)^2$ in Fig. 3b. In the new normalized distance the stress distributions for the four load levels collapse onto a single curve at distances beyond X_1^*. This suggests that, beyond the peak stress region, the field within the metal foil has the dependence $\sigma_{ij} = \sigma_0 q_{ij}(X_1/(K_I/\sigma_0)^2)$, as dictated by the remote K-field. On the other hand, the peak stress σ_m^* scales almost linearly with $K_I/\sqrt{h}$, with the proportionality constant depending primarily on E_s/E.

The normal stress σ_{22} exhibits the trends shown in Figs 2 and 3; it also peaks at X_1^*, the site of maximum mean stress. At distances beyond X_1^*, the variation of the stresses through the layer is negligible so that large normal tractions act across the interfaces between the metal foil and the substrates. The distribution of the stresses σ_{22}, σ_{12} and σ_{11} (in the metal foil and the ceramic) along the interfaces in Fig. 4 reveals high normal stresses but low shear stress. Within distances of several hs where

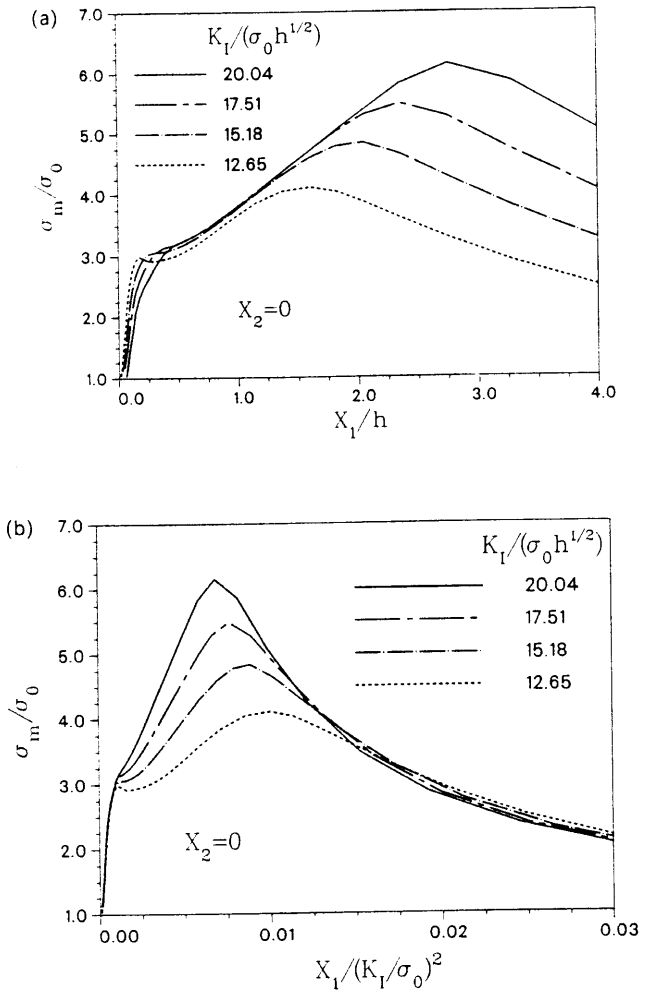

FIG. 3. Distribution of triaxiality along the crack ligament for various loading levels in the range of cavitation. (a) A second and higher peak stress develops at distance of several layer thickness ahead of the crack tip. (b) Beyond the peak stress, the field scales with K_I.

the plastic strains dominate, σ_{11} is higher in the metal foil. At larger distances, σ_{11} is higher in the ceramic and its magnitude approaches that of σ_{22} as required by the imposed mode I K-field.

The effect of material moduli on stress triaxiality is shown in Fig. 5. Under the same load, $K_I/(\sigma_0\sqrt{h}) = 12.65$, the difference in moduli has a pronounced effect on the peak stress—$\sigma_m^*(E_s/E = 1)$ is 25% higher than $\sigma_m^*(E_s/E = 5)$. At larger distances, $r \gg h$, where the fields are elastic, the difference increases to 40%. The latter figure can also be estimated by relation (B3) in Appendix B which was derived by taking into consideration the discontinuity of σ_{rr} across the interfaces. Material strain hardening has a slight effect on the peak stress. The finite element field shows that the

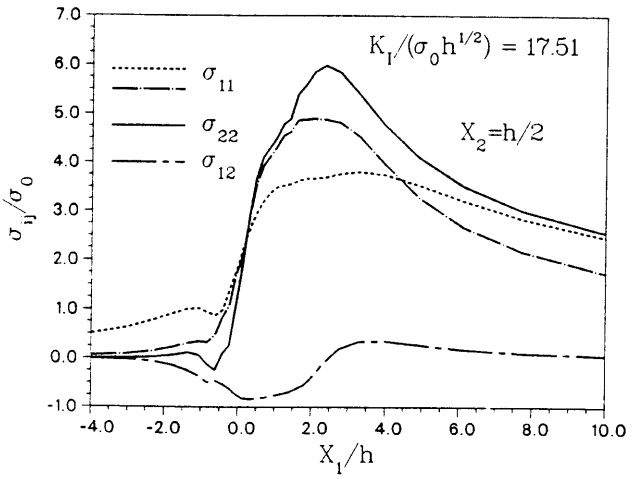

FIG. 4. Distribution of σ_{22}, σ_{12} and σ_{11} (--- of the ceramic; —·— of the metal foil) along the metal–ceramic interface.

maximum triaxiality, σ_m^*/σ_0, develops in a region of comparable elastic and plastic strains where strain hardening properties of the layer are of no consequence.

The maximum mean and normal stress, and the location X_1^* for five material combinations are given in Tables 1a–e. The loads are parameterized by $K_I/(\sigma_0\sqrt{h})$ or by $G/(\sigma_0 h)$, where G [see Eq. (4)] is the nominal energy-release rate. The material system with $E_s/E = 20$ is representative of a polymer layer bonded to metal substrates. For the loading range considered, which covers those of practical relevance, the distance X_1^* ranges between $1h$ and $4h$.

We have observed that σ_m^* scales almost linearly with $K_I/\sqrt{h}$. The proportionality constant, C_S, determined from the finite element results and relation (B4) of Appendix

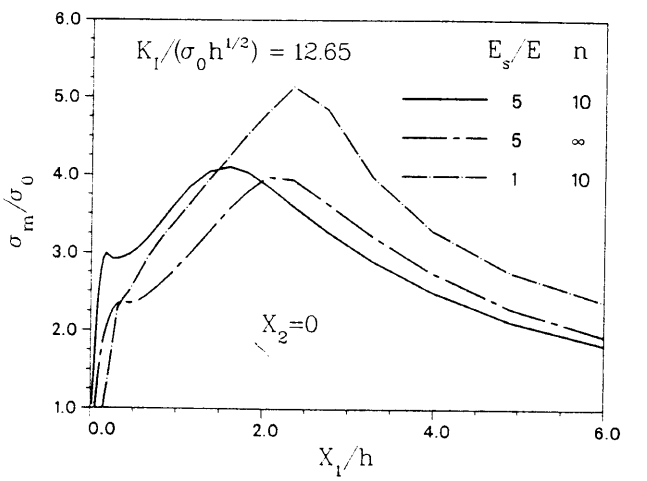

FIG. 5. Effect of material properties on the stress triaxiality.

TABLE 1. *Field quantities pertinent to metal foil failure.* σ_m^*: *maximum mean stress along the ligament.* σ_{22}^*: *maximum hoop stress along the ligament.* X_1^*: *position of* σ_m^* *and* σ_{22}^*. δ_t: *crack tip opening displacement*

TABLE 1a. $E/\sigma_0 = 300$, $\nu = 0.33$, $n = 10$, $\nu_s = 0.2$, $E_s/E = 1$

$K_I/(\sigma_0\sqrt{h})$	$G/(\sigma_0 h)$	σ_m^*/σ_0	X_1^*/h	σ_{22}^*/σ_0	$1/\bar{d}$
8.85	0.25	3.97	1.37	4.66	1.87
9.49	0.29	4.18	1.60	4.88	1.81
10.12	0.33	4.39	1.82	5.08	1.74
11.38	0.41	4.79	2.05	5.47	1.61
12.65	0.51	5.14	2.35	5.81	1.49

TABLE 1b. $E/\sigma_0 = 300$, $\nu = 0.33$, $n = 10$, $\nu_s = 0.2$, $E_s/E = 2$

$K_I/(\sigma_0\sqrt{h})$	$G/(\sigma_0 h)$	σ_m^*/σ_0	X_1^*/h	σ_{22}^*/σ_0	$1/\bar{d}$
10.23	0.17	4.06	1.37	4.76	1.99
13.20	0.28	5.02	2.05	5.71	1.76
15.14	0.37	5.51	2.35	6.18	1.60
16.41	0.43	5.92	2.75	6.59	1.50
17.21	0.47	6.00	3.28	6.70	1.45

TABLE 1c. $E/\sigma_0 = 300$, $\nu = 0.33$, $n = 10$, $\nu_s = 0.2$, $E_s/E = 5$

$K_I/(\sigma_0\sqrt{h})$	$G/(\sigma_0 h)$	σ_m^*/σ_0	X_1^*/h	σ_{22}^*/σ_0	$1/\bar{d}$
12.65	0.10	4.11	1.60	4.28	2.02
15.18	0.15	4.84	2.05	5.55	1.90
17.51	0.20	5.49	2.35	6.20	1.78
20.04	0.26	6.15	2.75	6.86	1.64
21.99	0.31	6.65	3.28	7.37	1.53

TABLE 1d. $E/\sigma_0 = 300$, $\nu = 0.33$, $n = \infty$, $\nu_s = 0.2$, $E_s/E = 5$

$K_I/(\sigma_0\sqrt{h})$	$G/(\sigma_0 h)$	σ_m^*/σ_0	X_1^*/h	σ_{22}^*/σ_0	$1/\bar{d}$
11.39	0.08	3.64	1.82	4.26	1.31
12.65	0.10	3.98	2.05	4.58	1.23
15.18	0.15	4.67	2.75	5.27	1.10
16.45	0.17	4.96	3.28	5.58	1.05
20.24	0.26	5.90	3.98	6.49	0.91

TABLE 1e. $E/\sigma_0 = 66.67$, $\nu = 0.33$, $n = 10$, $\nu_s = 0.33$, $E_s/E = 20$

$K_I/(\sigma_0\sqrt{h})$	$G/(\sigma_0 h)$	σ_m^*/σ_0	X_1^*/h	σ_{22}^*/σ_0	$1/\bar{d}$
12.66	0.11	2.56	1.16	3.23	1.74
14.90	0.15	3.01	1.38	3.69	1.73
17.14	0.20	3.46	1.79	4.14	1.67
19.38	0.25	3.90	1.96	4.59	1.58
21.62	0.31	4.35	2.45	5.03	1.49

TABLE 2. *Proportionality constants* C_S *and* C_X *in the cavitation range.* $E_f/\sigma_0 = 300$, $\nu = 0.33$, $\nu_s = 0.2$

Material properties		$C_S \equiv K_I/(\sigma^*_m\sqrt{h})$		$C_X \equiv K_I/(\sigma^*_{22}\sqrt{h})$
E_s/E	n	Finite elements	Relation (B4)	Finite elements
1	10	2.5	2.5	2.2
2	10	2.8	3.0	2.4
5	10	3.2	3.4	2.8
5	∞	3.2	3.4	2.8

B for four material combinations are tabulated in Table 2. It can be seen that the analytic estimates agree well with the finite element results. In the case of a system representative of metal–polymer, the finite element calculation yields $K_I/(\sigma^*_m\sqrt{h}) = 5.0$ while 3.7 is the value estimated by relation (B4). Likewise, σ^*_{22} nearly scales with $K_I/\sqrt{h}$ and the proportionality constant, C_X, is given in Table 2.

3.2. *Overall features of stresses*

It is useful to summarize the overall features of the fields. For $r_p < h$, the near-tip fields are nearly self-similar having the form

$$\sigma_{ij} = \sigma_0 h_{ij}\left(\frac{r}{J_{nf}/\sigma_0}, \theta\right). \tag{6}$$

For low to moderately hardening material, the maximum mean stress develops at about $3\delta_t$s ahead of the tip and does not exceed about $3\sigma_0$.

In the large-scale yielding regime, $r_p > h$, the maximum stresses scale with the applied load

$$\sigma^*_m = C_S^{-1} K_I/\sqrt{h}, \tag{7}$$

$$\sigma^*_{22} = C_X^{-1} K_I/\sqrt{h}, \tag{8}$$

where C_S and C_X are weakly dependent on E_s/E and are given in Table 2. The peak stresses develop at distances of several foil thicknesses ahead of the tip, and increase continuously with applied load until an intervening failure mechanism becomes operative. In the interval $3\delta_t < X_1 < X_1^*$, the mean and normal stresses along the centerline, increase almost linearly with distance (see Fig. 3a), behaving like $(\sigma_m, \sigma_{22}) \propto \sigma_0 X_1/h$. The proportionality constants depend on strain hardening and E_s/E. Beyond the peak stress region, $X_1 > X_1^*$, the X_1 variation of the stresses in the foil has the form

$$\sigma_{ij} = \sigma_0 q_{ij}\left(\frac{X_1}{(K_I/\sigma_0)^2}\right). \tag{9}$$

Self-similar fields of the form in Eq. (6) for non-hardening and low to moderately hardening materials have been discussed by MCMEEKING (1977). These self-similar fields have been shown by O'DOWD and SHIH (1991) to be a particular member of a

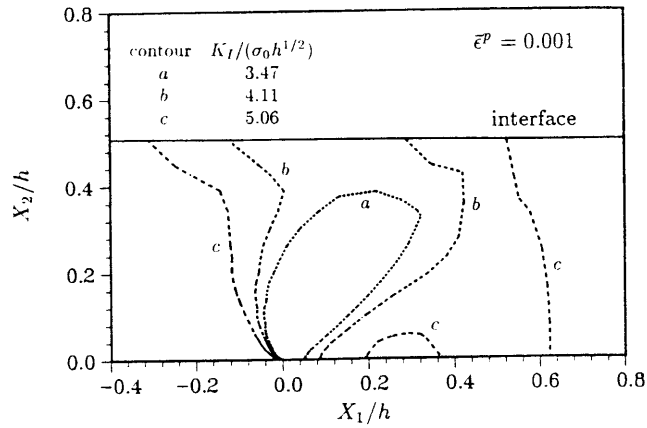

FIG. 6. Evolution of the plastic zone constrained by elastic substrates.

family of crack-tip fields which can be obtained by applying a tensile (or compressive) stress parallel to the crack plane; indeed their high- and ultra-high-triaxiality stress fields are similar to the fields shown in Figs 2 and 3. We note that stress triaxiality can also be elevated by partially constrained large-scale plastic flow. For example, plastic flow emanating from an interface crack and constrained by the boundary of an elastic substrate can elevate the mean stress by as much as 40% beyond the level that develops in a homogeneous material (SHIH *et al.*, 1991).

4. DEVELOPMENT OF PLASTICITY FIELDS

4.1. *Growth of plastic zone*

Under small-scale yielding conditions, $r_p \ll h$, the calculated plastic zone size follows the known form $r_p = 0.15(K/\sigma_0)^2$. Upon coming into contact with the stiff elastic substrates the plastic zone is constrained and spreads laterally. The evolution of the plastic zone in the metal foil for the system described by Eq. (2) is shown in Fig. 6. The growth of the plastic zone with applied load $K_I/(\sigma_0\sqrt{h})$ is shown in Fig. 7. In the range $r_p \gg h$, the plastic zone size scales linearly with $(K_I/\sigma_0)^2$. The proportionality constant depends on the ratio of the Young's moduli, E_s/E, and Poisson's ratios of the foil and the substrates. Table 3 compares the proportionality constants, determined from the finite element results and that given by relation (B5) of Appendix B, for $E/\sigma_0 = 300$, $\nu = 0.33$ and $\nu_s = 0.2$. The good agreement is noted. For the metal–polymer system in which the mismatch of the elastic moduli is very large, the finite element solution gives $r_p/(K_I/\sigma_0)^2 = 0.055$, while the analytic prediction is 0.038.

4.2. *Crack-tip shielding*

The value of the J-integral is calculated for contours of increasing mean radius around the crack tip by the domain-integral method of LI *et al.* (1985). The value of

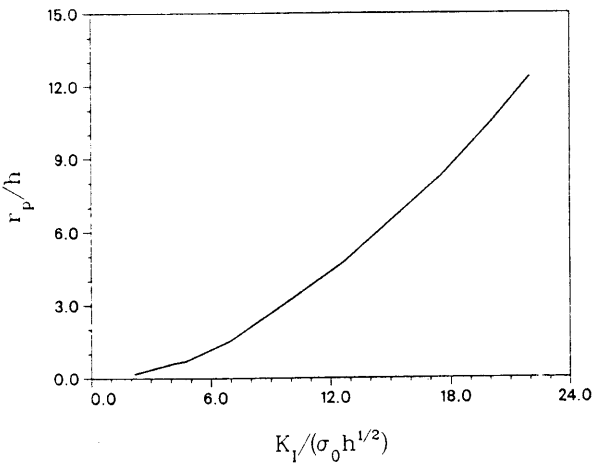

FIG. 7. Growth of plastic zone size with applied load.

TABLE 3. *Proportionality constant*, $r_p/(K_I/\sigma_0)^2$, *in the range* $r_p \gg h$. $E/\sigma_0 = 300$, $\nu = 0.33$, $\nu_s = 0.2$

Material properties		$r_p/(K_I/\sigma_0)^2$	
E_s/E	n	Finite elements	Relation (B5)
1	10	0.031	0.035
2	10	0.019	0.018
5	10	0.025	0.027
5	∞	0.029	0.027

J normalized by G (which is also J_{remote}) versus the mean radial distance of the annular strip of elements from the tip is shown in Fig. 8 for four levels of applied load. For $K_I/(\sigma_0\sqrt{h}) < 2.5$, where $r_p < h/4$, J is path-independent everywhere excluding the crack-tip region $r < 5\delta_t$, i.e., $J_{\text{nf}} = J_{\text{remote}}\ (= G)$.

As the plastic zone size increases, path-independence of J is preserved in two distinct regions, $5\delta_t < r < r_p$ (or h whichever is smaller) and $h \ll r < L$ (L is the distance to the load point) but $J_{\text{nf}} \neq J_{\text{remote}}\ (= G)$. The inner annulus, referred to as the near-field or local J-annulus, lies wholly within the plastic zone while the outer or remote annulus lies at distances large compared to the foil thickness. The shielding of the crack tip, $J_{\text{nf}} < J_{\text{remote}}$, is the consequence of the non-proportional stressing associated with the plastic flow in the metal foil being constrained by the substrates. The deviation of J_{nf} from J_{remote} can be seen in the curves for $K_I/(\sigma_0\sqrt{h}) = 5.06$, 6.96 and 10.12. For these three cases, J_{nf} is defined by the mean value of J within the annulus $0.1 < r/h < 0.4$.

The practical significance of crack-tip shielding may be appreciated in the following way. Imagine a fracture test of a ductile adhesive joint, with the layer thickness of the order of the critical plastic zone size tested in bulk. Under remote loading, the crack

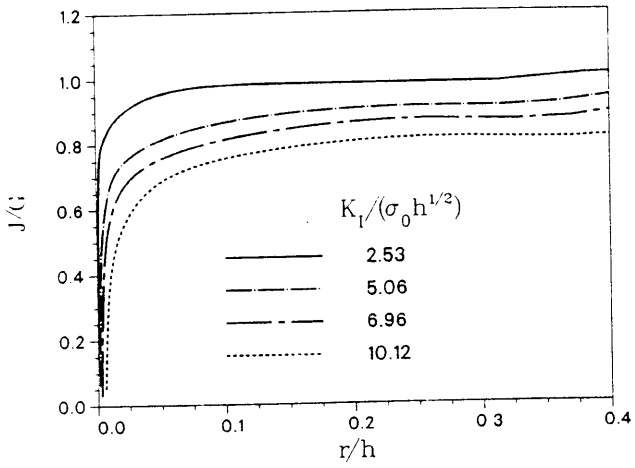

FIG. 8. The J-integral evaluated near the tip is plotted against the mean radii of the integration paths. The local annulus in which the J-integral is path-independent can be seen.

advances when J_{nf} attains the bulk toughness of the adhesive J_C, provided that the material properties of the adhesive are not modified in the joining process. The shielding implies that the measured nominal fracture energy of the joint, G_C, will be higher than the bulk toughness J_C of the adhesive. Indeed, an increase of the nominal fracture energy for certain adhesive thicknesses has been observed experimentally (e.g. BASCOM *et al.*, 1975; BASCOM and COTTINGTON, 1976; CHAI, 1986).

The shielding described above is different from the shielding of near-tip K from remote K_I due to large mismatch of elastic moduli, E_s/E [see Eq. (5)], which has been observed in brittle adhesive joints such as glass adhesives used to join ceramic components (FLECK *et al.*, 1990; SUO, 1990).

4.3. *Crack-tip blunting*

Under small-scale yielding, a relationship of the form $\delta_t = d(\varepsilon_0, n)J/\sigma_0$ has been shown for bulk metals. Here δ_t is the opening separation where the 45° lines, drawn backwards from the crack tip, intercept the deformed crack faces, and d is a proportionality factor which depends strongly on n and weakly on ε_0 (SHIH, 1981). For the constrained metal foil, δ_t is almost linear with J_{nf}

$$\delta_t = \hat{d}(\varepsilon_0, n)\frac{J_{nf}}{\sigma_0}, \tag{10}$$

where $\hat{d}$ depends additionally on the parameters of the system, e.g., E_s/E, r_p/h. Under small-scale yielding, $\hat{d} = d$.

The variation of δ_t/h, and δ_t normalized by (G/σ_0) with applied load is shown in Fig. 9. In this plot, δ_t is twice the displacement of point A along the X_2-axis, where A is the intersection of the straight flank and the curved notch surface in the undeformed configuration (see Fig. 10 of Appendix A). In the context of this boundary value

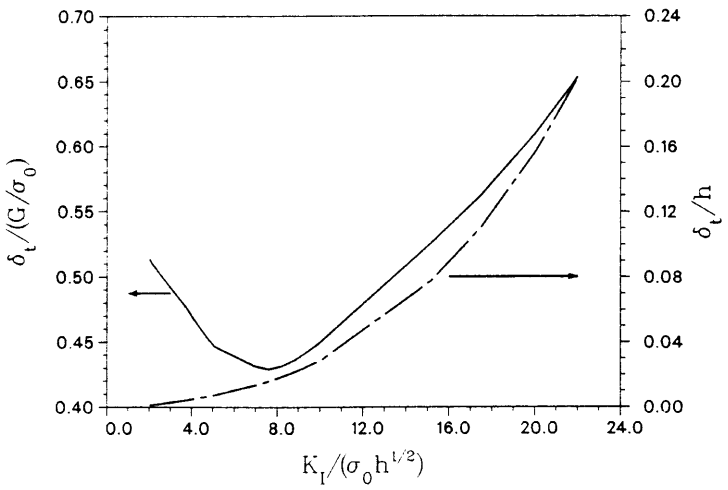

FIG. 9. Variation of crack tip opening displacement with the applied load.

problem, δ_t scales linearly with G/σ_0 only if $r_p \ll h$. For $K = 2.02\sigma_0\sqrt{h}$ and $r_p = 0.15h$, $\delta_t/(G/\sigma_0)$ is equal to 0.51, which agrees well with the value of 0.52 for a bulk material with the properties of the foil (SHIH, 1981). As the plastic zone expands, this ratio decreases initially, reaching a minimum for $r_p \approx 2h$ and then increases again. The initial decrease is a consequence of the shielding of the crack tip by constrained plastic flow. With higher applied loads, the highly constrained large scale plastic flow ($r_p \gg h$) elevates the mean stress in the foil which results in the δ_t increasing at a faster rate than G/σ_0. The ratios $G/(\sigma_0\delta_t)$ ($\equiv 1/\bar{d}$) are given in Tables 1a–e for several material systems.

5. COMPETING FAILURE MECHANISMS

The maximum mean stresses that can develop within a metal foil are much higher than those associated with an isolated crack in the corresponding bulk metal. This response makes the constrained foil susceptible to failure mechanisms associated with high normal stresses. The competition of three potential mechanisms are considered here. They are: (i) near-tip void growth at second-phase particles or interfacial pores and coalescence with the main crack, (ii) high-triaxiality cavitation, i.e., nucleation and rapid void growth at highly stressed sites at distances of several layer thicknesses from the crack tip, and (iii) interfacial debonding at the site of highest normal interfacial traction.

Crack advance by growth and coalescence of near-tip voids with the crack is a typical ductile fracture mechanism. Voids in the present context can be either those nucleated around second phase particles in the metal foil or residual pores on the interface formed in the processing. In particular, when the crack tip blunts to an opening of the order of the mean spacing between voids, X_0, the voids are wholly

within the finite strain zone so that void-crack coalescence is imminent (e.g. RICE and JOHNSON, 1970). Combining the growth criterion

$$\delta_t = X_0 \tag{11a}$$

with $G/(\sigma_0\delta_t) = 1/\bar{d}$ leads to a relation for the critical nominal energy-release rate for such void-crack coalescence

$$G_C = (1/\bar{d})\sigma_0 X_0. \tag{11b}$$

The values for $1/\bar{d}$ can be found in the last column in Tables 1a–e. For the material system described by Eq. (2), $1/\bar{d}$ decreases from about 2.0 to 1.5 as the plastic zone size increases from a fraction of h to several hs.

In very thin foils, cavitation at the site of high triaxial stresses at distances of several hs ahead of the crack tip may precede coalescence. According to HUANG *et al.* (1990), a void in an elastic–plastic material will grow unstably when the mean stress reaches $C_N\sigma_0$ where the cavitation number $C_N = 5.5$ for a metal with the properties given in Eq. (2). We have observed that the ratio $K_I/(\sigma^*_m\sqrt{h})$ designated by C_S remains nearly constant with increasing loading and can be considered a property of the system, depending primarily on E_s/E (see Table 2). Combining the two results, we have

$$K_{IC} = C_S C_N \sigma_0 \sqrt{h}, \tag{12a}$$

and an equivalent relation for the critical nominal energy release rate takes the form

$$G_C = \left[C_S^2 C_N^2 \varepsilon_0 \left(\frac{(1-\nu_s^2)E}{E_s}\right)\right]\sigma_0 h. \tag{12b}$$

As an example, for a system having the properties given in Eq. (2), the result is $G_C = 0.2\sigma_0 h$.

Suppose the crack geometry is loaded to the point where cavitation at $r > h$ is imminent. Using the values in Tables 1 and 2, and relations (11b) and (12b), we estimated the critical nominal energy release rates required to drive mechanisms (i) and (ii) for four material combinations. These are tabulated in Table 4 (the estimates in the third column are based on values of $1/\bar{d}$ appropriate to $\sigma_m = C_N\sigma_0$). Consider the material combination given by Eq. (2), where $G_C/(\sigma_0 X_0) = 1.8$ for coalescence and $G_C/(\sigma_0 h) = 0.2$ for cavitation. Since the operative mechanism is the one requiring

TABLE 4. *Comparison of critical energy release rates* G_C, $G_C/(\sigma_0 h)$: *critical ratio for triggering cavitation,* $G_C/(\sigma_0 X_0)$: *critical ratio for void coalescence.* $E/\sigma_0 = 300$, $\nu = 0.33$, $\nu_s = 0.2$

E_s/E	n	$G_C/(\sigma_0 X_0)$	$G_C/(\sigma_0 h)$
1	10	1.5	0.6
2	10	1.6	0.4
5	10	1.8	0.2
5	∞	1.2	0.1

a smaller G_C, we conclude that high-triaxiality cavitation develops if $h/X_0 < 9$, while the near-tip void coalescence mechanism is operative if $h/X_0 > 9$. It may be noted that the critical value of h/X_0 depends on E/E_s as can be seen in Table 4.

The system parameter which affects the competition between the two mechanisms is given by the ratio of the right-hand side in Eq. (12b) to that in (11b), i.e., high-triaxiality cavitation dominates if

$$[C_S^2 C_X^2 \varepsilon_0 (1-\nu_s^2)\bar{d}] \frac{Eh}{E_s X_0} < 1. \tag{13}$$

Since the quantities within the brackets depend only weakly on E_s/E, we may conclude that increasing the substrate stiffness, but keeping the other properties and the geometry fixed, increases the likelihood of high-triaxiality cavitation.

The third mechanism is operative when the tensile traction across the interface reaches the critical value $C_A\sigma_0$. Values for C_A, the coefficient of adhesion, in the range 3–10 have been reported for inclusion matrix interface in steels and Cu–0.6%–Cr alloy (ARGON and IM, 1975; CIALONE and ASARO, 1981). In the range $r_p > h$, the ratio $K_I/(\sigma_{22}^* \sqrt{h})$ designated by C_X changes slowly with applied load and is nearly a system property depending primarily on E_s/E (see Table 2). Combining these results, we have

$$K_{IC} = C_X C_A \sigma_0 \sqrt{h} \tag{14a}$$

and

$$G_C = \left[C_X^2 C_A^2 \varepsilon_0 \left(\frac{(1-\nu_s^2)E}{E_s} \right) \right] \sigma_0 h. \tag{14b}$$

The competition between mechanisms (i) and (iii) can be quantified following the above procedure, i.e., interfacial debonding at $r > h$ is operative if

$$[C_S^2 C_A^2 \varepsilon_0 (1-\nu_s^2)\bar{d}] \frac{Eh}{E_s X_0} < 1. \tag{15}$$

Likewise interfacial debonding dominates over mechanism (ii) if

$$\frac{C_X C_A}{C_S C_V} < 1. \tag{16}$$

It warrants emphasis that G_C in Eqs (12b) and (14b) corresponds to the critical energy release rate for triggering the first cavitation and debonding respectively. For example, REIMANIS and EVANS (1991) have observed that before the ligament bridging the first cavity to the crack tip ruptures, several arrays of cavities parallel to the crack front nucleate in sequence as the applied load increases; more cavities are nucleated after ligament rupture and the process repeats itself. Thus the value of G_C in (12b) and (14b) as well as the fourth column of Table 4 are critical energy release rates for initial cavitation and debonding and should not be regarded as the steady-state fracture energies.

The material and system parameters that can affect the competition between the three mechanisms are shown in Eqs (13), (15) and (16). The quantities within the

brackets in Eqs (13) and (15) are only weakly dependent on E_s/E. Thus the inequalities in Eqs (13) and (15) show that increasing the substrate stiffness relative to the foil stiffness favors the development of mechanisms (ii) and (iii). Similarly decreasing the layer thickness while maintaining the material properties of the system also favors mechanisms (ii) and (iii). When the substrate endures large stresses cleavage fracture of the ceramic is a possible mode of fracture. For example, if the stresses necessary for cavitation exceed the strength of the ceramic, failure by cleavage of the ceramic may intervene.

6. CONCLUDING REMARKS

A variety of failure behaviors have been observed for ductile metal foils constrained between elastic blocks. For material combinations and/or processing methods which result in low-strength interfacial bonding, de-adhesion of metal–ceramic interface accompanied by plastic deformation is the dominant separation mechanism. Systems such as copper–glass (OH *et al.*, 1987), platinum–alumina (DALGLEISH *et al.*, 1988), gold–sapphire (REIMANIS *et al.*, 1990), with respective testing conditions, appear to belong to this type. For such systems, relatively large fracture energies compared with the work of adhesion are usually measured, which may be attributed to the work dissipated by the local plastic deformation in the metal foil. The nominal fracture energy can be further enhanced by modifying interface geometry to encourage partial debonding and large plastic stretching of metal foils (OH *et al.*, 1988).

When the interface bond strength is high, the three mechanisms discussed in Section 5 as well as ceramic cleavage must be included as potential mechanisms. For example, systems such as aluminum–alumina (DALGLEISH *et al.*, 1989) and gold–sapphire (REIMANIS and EVANS, 1991) develop failure modes described in (ii) and (iii). Indeed the high normal interfacial tractions that develop in geometries of the type depicted in Fig. 1 suggests that interfacial debonding as a dominant failure mode is highly favored. The quantitative connection between the nominal fracture energy and de-adhesion at large distances from the tip can be studied by using the de-adhesion models investigated by NEEDLEMAN (1987) and VARIAS *et al.* (1990a, b).

Constrained metal deformation is a generic feature for most ductile–brittle composites. The metal foil bonded between ceramic substrates provides a convenient experimental set-up for studying a variety of failure mechanisms. A way to evaluate the multi-mechanism competition is to estimate fracture energy for each mechanism, with the understanding that the mechanism requiring lowest fracture energy would become operative. Along this line we have carried out an evaluation of the multi-mechanism competition using the results of a full-field finite deformation analysis of the metal foil crack geometry.

Several issues requiring analysis include the effects of mode mixity of the applied load, residual stress, and de-adhesion of metal–ceramic interfaces on the distribution of near-tip fields and interfacial tractions and on the elevation of the mean stress. Such information is necessary for the interpretation of existing test data discussed above. For example, our results for mixed mode loading show that significantly larger plastic zone sizes r_p/h are required to generate the range of stress triaxialities discussed

in this paper. This means that the nominal fracture toughness under mixed mode loading should be larger than that for mode I loading, assuming that failure is governed by the same mechanism. Investigations along these lines are in progress. Experiments should be conducted under mode I remote load using pure metal foils with high adhesion and low residual stress; such data are more readily interpreted. These coordinated efforts would provide the necessary validation to ascertain cavitation as a distinct failure mechanisms and the parameters that govern the competition between the various mechanisms.

Acknowledgements

The authors are grateful to A. G. Evans and J. W. Hutchinson for stimulating discussions. A.G.V. and C.F.S. are supported by the Office of Naval Research through a grant on "Mechanics of Interface Cracks." Z.S. is supported by ONR (contract N00014-85-K-0883) and by NSF (MSS-9011571). The computations were performed on the Alliant Computer in the Computational Mechanics Facility of Brown University. The acquisition of the Alliant was made possible by grants from the U.S. National Science Foundation (grant DMR-8714665), and the Office of Naval Research/DARPA (grant N00014-88-K-0119), and matching funds from Brown University.

References

Argon, A. S. and Im, J. 1975 *Metall. Trans.* **6A**, 839.

Ashby, M. F., Blunt, F. J. and Bannister, M. 1989 *Acta Metall.* **37**, 1847.

Bascom, W. D. and Cottington, R. L. 1976 *J. Adhesion* **7**, 333.

Bascom, W. D., Cottington, R. L., Jones, R. L. and Peyser, P. 1975 *J. Appl. Polymer Sci.* **19**, 2545.

Chai, H. 1986 *Composite Materials: Testing and Design (Seventh Conference)*, ASTM STP 893, p. 209 (edited by J. M. Whitney). American Society for Testing and Materials, Philadelphia.

Cialone, H. and Asaro, R. J. 1981 *Metall. Trans.* **12A**, 1373.

Dalgleish, B. J., Lu, M. C. and Evans, A. G. 1988 *Acta Metall.* **36**, 2029.

Dalgleish, B. J., Trumble, K. P. and Evans, A. G. 1989 *Acta Metall.* **37**, 1923.

Fleck, N. A., Hutchinson, J. W. and Suo, Z. 1991 *Int. J. Solids Struct.* **27**, 1683.

Harren, S. V., Deve, H. E. and Asaro, R. J. 1988 *Acta Metall.* **36**, 2435.

Huang, Y., Hutchinson, J. W. and Tvergaard, V. 1990 Harvard University, report MECH-153.

Li, F. Z., Shih, C. F. and Needleman, A. 1985 *Engng Fracture Mech.* **21**, 405.

McMeeking, R. M. 1977 *J. Mech. Phys. Solids* **25**, 357.

Needleman, A. 1987 *J. appl. Mech.* **54**, 525.

O'Dowd, N. P. and Shih, C. F. 1991 *J. Mech. Phys. Solids* (In press).

OH, T. S., CANNON, R. M. and RITCHIE, R. O. 1987 *J. Am. Ceram. Soc.* **70**, C-352.
OH, T. S., RODEL, J., CANNON, R. M. and RITCHIE, R. O. 1988 *Acta Metall.* **36**, 2083.
PEIRCE, D., ASARO, R. J. and NEEDLEMAN, A. 1983 *Acta Metall.* **31**, 1951.
PEIRCE, D., SHIH, C. F. and NEEDLEMAN, A. 1984 *Comput. Struct.* **18**, 875.
REIMANIS, I. E. and EVANS, A. G. 1991 *Acta Metall. Mater.* (In press).
REIMANIS, I. E., DALGLEISH, B. J., BRAHY, M., RUHLE, M. and EVANS, A. G. 1990 *Acta Metall. Mater.* **38**, 2645.
RICE, J. R. 1968 *J. appl. Mech.* **35**, 379.
RICE, J. R. and JOHNSON, M. A. 1970 *Inelastic Behavior of Solids*, p. 641 (edited by M. F. KANNINEN, W. F. ADLER, A. R. ROSENFIELD and R. I. JAFFEE). McGraw-Hill, New York.
SHIH, C. F. 1981 *J. Mech. Phys. Solids* **29**, 305.
SHIH, C. F., ASARO R. J. and O'DOWD, N. P. 1991 *J. appl. Mech.* (In press).
SUO, Z. 1990 *Appl. Mech. Rev.* **43**, 276.
VARIAS, A. G., O'DOWD, N. P., ASARO, R. J. and SHIH, C. F. 1990a *Materials Science and Engineering* **A126**, 65.
VARIAS, A. G., O'DOWD, N. P., MCHUGH, P. E. and SHIH, C. F. 1990b *Proceedings of* 1990 *ASME International Computers In Engineering Conference*, Vol. 2, p. 671 (edited by G. L. KINZEL and S. M. ROHDE). Boston.

APPENDIX A

Standard tensor notation is used throughout. Bold-faced symbols are used to denote vectors and higher-order tensors, the orders of which will be clear in context. Products are indicated with dots and products containing no dots are diadic products. Latin indices range from one to the number of spatial dimensions and repeated Latin indices are always summed. Inverses, transposes and transposed inverses are denoted with a superscripted -1, T and $-T$, respectively, and superposed dots indicate differentiation with respect to time t. For instance

$$\mathbf{A}\cdot\mathbf{B} = A_{ik}B_{kj}\mathbf{b}_i\mathbf{b}_j, \qquad \mathbf{A}:\mathbf{B} = A_{ij}B_{ij},$$

$$\mathbf{cd} = c_ic_j\mathbf{b}_i\mathbf{b}_j, \qquad \mathbf{c}\cdot\mathbf{d} = c_id_i,$$

$$\mathbf{H}:\mathbf{A} = H_{ijkl}A_{lk}\mathbf{b}_i\mathbf{b}_j, \qquad \mathbf{A}:\mathbf{H} = A_{kl}H_{lkij}\mathbf{b}_i\mathbf{b}_j,$$

$$\dot{\mathbf{B}} = \frac{\partial B_{ij}}{\partial t}\mathbf{b}_i\mathbf{b}_j, \qquad \mathbf{B}\cdot\mathbf{c} = B_{ik}c_k\mathbf{b}_i,$$

where the base vectors, $\mathbf{b}_i$, are Cartesian and independent of time.

Material constitutive relations

The deformation gradient is taken to be multiplicably decomposable into elastic and plastic parts, via

$$\mathbf{F} = \partial\mathbf{x}/\partial\mathbf{X} = \mathbf{F}^*\cdot\mathbf{F}^p, \tag{A1}$$

where $\mathbf{x}$ is the current position of a material particle and $\mathbf{X}$ is its position in a reference state.

$\mathbf{F}^p$ is the deformation due solely to the plastic flow and $\mathbf{F}^*$ is the remaining contribution to $\mathbf{F}$ associated with elastic distortion and any rigid rotation of the material. The velocity gradient is of the form

$$\mathbf{L} = \dot{\mathbf{F}} \cdot \mathbf{F}^{-1} = \dot{\mathbf{F}}^* \cdot \mathbf{F}^{*-1} + \mathbf{F}^* \cdot \dot{\mathbf{F}}^p \cdot \mathbf{F}^{p-1} \cdot \mathbf{F}^{*-1}. \tag{A2}$$

This leads to plastic and elastic parts of the rate of deformation $\mathbf{D}$ given by

$$\mathbf{D} = \text{sym}(\mathbf{L}) = \mathbf{D}^p + \mathbf{D}^* = \mathbf{F}^* \cdot \dot{\mathbf{F}}^p \cdot \mathbf{F}^{p-1} \cdot \mathbf{F}^{*-1} + \text{sym}(\dot{\mathbf{F}}^* \cdot \mathbf{F}^{*-1}), \tag{A3}$$

while the spin $\mathbf{W}$ is only due to $\mathbf{F}^*$ and is given by the relation

$$\mathbf{W} = \text{skew}(\mathbf{L}) = \text{skew}(\dot{\mathbf{F}}^* \cdot \mathbf{F}^{*-1}). \tag{A4}$$

The elastic response is expressed in terms of the Lagrangian strain $\mathbf{E}^*$, and the second Piola–Kirchhoff stress $\mathbf{S}^*$, which are defined by the following relations

$$\mathbf{E}^* = \tfrac{1}{2}(\mathbf{F}^{*T} \cdot \mathbf{F}^* - \mathbf{I}), \tag{A5a}$$

$$\mathbf{S}^* = \mathbf{F}^{*-1} \cdot \boldsymbol{\tau} \cdot \mathbf{F}^{*-T}, \tag{A5b}$$

where $\boldsymbol{\tau} = (\det \mathbf{F})\boldsymbol{\sigma}$ is the Kirchhoff stress and $\boldsymbol{\sigma}$ is the Cauchy stress. $\mathbf{S}^*$ is the second Piola–Kirchhoff stress on the intermediate configuration, which is obtained by applying the mapping $\mathbf{F}^p$ to the reference configuration. A strain energy function, Φ, is assumed to exist which requires

$$\mathbf{S}^* = \frac{\partial \Phi}{\partial \mathbf{E}^*}. \tag{A6}$$

In rate form the elasticity relations are

$$\dot{\mathbf{S}}^* = \mathbf{K} : \dot{\mathbf{E}}^*, \qquad \mathbf{K} = \frac{\partial^2 \Phi}{\partial E^*_{ij} \partial E^*_{kl}} \mathbf{b}_i \mathbf{b}_j \mathbf{b}_k \mathbf{b}_l. \tag{A7}$$

In this study, the elastic potential Φ is taken as

$$\begin{aligned} \Phi = {} & \tfrac{1}{2}\lambda(E^*_{11} + E^*_{22} + E^*_{33})^2 + \mu(E^{*2}_{11} + E^{*2}_{22} + E^{*2}_{33}) \\ & + \tfrac{1}{2}\mu[(E^*_{12} + E^*_{21})^2 + (E^*_{23} + E^*_{32})^2 + (E^*_{31} + E^*_{13})^2], \end{aligned} \tag{A8}$$

where λ and μ are the Lamé constants.

The plastic response is specified by the flow rule, which takes the form

$$\mathbf{D}^p = \dot{\bar{\varepsilon}}^p \mathbf{p}, \tag{A9}$$

where

$$\mathbf{p} = \frac{3}{2} \frac{\boldsymbol{\tau}'}{\bar{\sigma}}, \tag{A10a}$$

$$\boldsymbol{\tau}' = \boldsymbol{\tau} - \tfrac{1}{3}\,\text{tr}(\boldsymbol{\tau})\mathbf{I}, \tag{A10b}$$

$$\bar{\sigma}^2 = \tfrac{3}{2}\boldsymbol{\tau}' : \boldsymbol{\tau}' = \tfrac{3}{2}(\mathbf{S}^{*\prime} \cdot \mathbf{C}^*) : (\mathbf{S}^{*\prime} \cdot \mathbf{C}^*), \tag{A10c}$$

$$\mathbf{S}^{*\prime} = \mathbf{S}^* - \tfrac{1}{3}(\mathbf{S}^* : \mathbf{C}^*)\mathbf{C}^{*-1}. \tag{A10d}$$

$\boldsymbol{\tau}'$ and $\mathbf{S}^{*\prime}$ are the deviatoric parts of $\boldsymbol{\tau}$ and $\mathbf{S}^*$, respectively. $\mathbf{C}^* = \mathbf{F}^{*T} \cdot \mathbf{F}^*$ is the elastic Cauchy–Green tensor and $\dot{\bar{\varepsilon}}^p$ is the effective plastic strain rate. In the present work, power law material strain rate sensitivity and strain hardening were assumed in the form

$$\dot{\bar{\varepsilon}}^p = \dot{\varepsilon}_0 \left(\frac{\bar{\sigma}}{H(\bar{\varepsilon}^p)} \right)^{1/m}. \tag{A11}$$

We assume that $H(\bar{\varepsilon}^p)$ evolves according to an isotropic hardening relation

$$H(\bar{\varepsilon}^p) = \sigma_0\left(1+\frac{\bar{\varepsilon}^p}{\varepsilon_0}\right)^{1/n}, \tag{A12}$$

where n is a hardening exponent, σ_0 is a reference stress, ε_0 ($=\sigma_0/E$) and $\dot{\varepsilon}_0$ are reference strain and strain rate, respectively and m is the rate-sensitivity exponent.

The above constitutive relations can be combined to provide a relation between the rate of the second Piola–Kirchhoff stress on the reference configurations, $\mathbf{S} = \mathbf{F}^{-1}\cdot\boldsymbol{\tau}\cdot\mathbf{F}^{-T}$, and the rate of the total Lagrangian strain, $\mathbf{E} = \frac{1}{2}(\mathbf{F}^T\cdot\mathbf{F}-\mathbf{I})$. Straightforward algebraic manipulations lead to the following relations

$$\dot{\mathbf{E}}^* = \mathbf{F}^{p-T}\cdot\dot{\mathbf{E}}\cdot\mathbf{F}^{p-1} - \dot{\bar{\varepsilon}}^p\mathbf{A}, \tag{A13a}$$

$$\dot{\mathbf{S}}^* = \mathbf{F}^p\cdot\dot{\mathbf{S}}\cdot\mathbf{F}^{pT} + 2\dot{\bar{\varepsilon}}^p\mathbf{B}, \tag{A13b}$$

where

$$\mathbf{A} = \frac{3}{2\bar{\sigma}}(\mathbf{C}^*\cdot\mathbf{S}^{*\prime}\cdot\mathbf{C}^*), \tag{A14a}$$

$$\mathbf{B} = \frac{3}{2\bar{\sigma}}(\mathbf{S}^{*\prime}\cdot\mathbf{C}^*\cdot\mathbf{S}^*). \tag{A14b}$$

Substituting relations (A13) into the first of the relations (A7), we finally obtain the complete constitutive relation in terms of the rates of $\mathbf{E}$ and $\mathbf{S}$

$$\dot{\mathbf{S}} = \mathbf{L}:\dot{\mathbf{E}} - \dot{\bar{\varepsilon}}^p\mathbf{Y}, \tag{A15}$$

where

$$\mathbf{L} = F^{p-1}_{ik}F^{p-1}_{jl}K_{klpq}F^{p-1}_{rp}F^{p-1}_{nq}\mathbf{b}_i\mathbf{b}_j\mathbf{b}_r\mathbf{b}_n, \tag{A16}$$

and

$$\mathbf{Y} = \mathbf{F}^{p-1}\cdot\{\mathbf{K}:\mathbf{A}+2\mathbf{B}\}\cdot\mathbf{F}^{p-T}. \tag{A17}$$

Relations (A13) and (A15)–(A17) are similar to those developed for crystal plasticity (HARREN *et al.*, 1988; VARIAS *et al.*, 1990a).

Finite element implementation

The rate constitutive relation (A15) is implemented via the one step, explicit method of PIERCE *et al.* (1983, 1984). The increment of the effective plastic strain is defined by the following relation, where a linear interpolation within the time increment is also employed

$$\Delta\bar{\varepsilon}^p = \bar{\varepsilon}^p(t+\Delta t) - \bar{\varepsilon}^p(t) = \Delta t[(1-\theta)\dot{\bar{\varepsilon}}^p_t + \theta\dot{\bar{\varepsilon}}^p_{t-\Delta t}]. \tag{A18}$$

The subscript denotes the time at which the plastic strain rates are evaluated. The parameter θ takes values from 0 to 1; $\theta = 0$ corresponds to a simple Euler time integration scheme. The strain rate at time $t+\Delta t$ is approximated by a Taylor expansion

$$\dot{\bar{\varepsilon}}^p_{t+\Delta t} = \dot{\bar{\varepsilon}}^p_t + \frac{\partial\dot{\bar{\varepsilon}}^p}{\partial\bar{\sigma}}\Delta\bar{\sigma} + \frac{\partial\dot{\bar{\varepsilon}}^p}{\partial\bar{\varepsilon}^p}\Delta\bar{\varepsilon}^p. \tag{A19}$$

The increment of the effective stress, $\bar{\sigma}$, is obtained from relation (A10c)

$$\Delta\bar{\sigma} = \dot{\bar{\sigma}}\Delta t = (\mathbf{Y}:\dot{\mathbf{E}})\Delta t - (\mathbf{R}:\mathbf{A})\Delta\bar{\varepsilon}^p, \tag{A20}$$

where

$$\mathbf{R} = \mathbf{K}:\mathbf{A}+2\mathbf{B}. \tag{A21}$$

$\mathbf{A}$ and $\mathbf{B}$ are defined by relations (A14). Combining relations (A18)–(A20), we get the expression for the average plastic strain rate in the time interval Δt

$$\frac{\Delta\bar{\varepsilon}^p}{\Delta t} = \frac{1}{\Pi}\left[\dot{\bar{\varepsilon}}_t^p + \Delta t\theta \frac{\partial\dot{\bar{\varepsilon}}^p}{\partial\bar{\sigma}}(\mathbf{Y}:\dot{\mathbf{E}})\right], \tag{A22}$$

where

$$\Pi = 1 + \theta\Delta t\left(\frac{\partial\dot{\bar{\varepsilon}}^p}{\partial\bar{\sigma}}\mathbf{R}:\mathbf{A} - \frac{\partial\dot{\bar{\varepsilon}}^p}{\partial\bar{\varepsilon}^p}\right). \tag{A23}$$

The calculated average plastic strain rate is substituted into the constitutive relation (A15) and its time discrete form is derived

$$\dot{\mathbf{S}} = \mathbf{L}^{\tan}:\dot{\mathbf{E}} - \frac{\dot{\bar{\varepsilon}}_t^p}{\Pi}\mathbf{Y}, \tag{A24}$$

where

$$\mathbf{L}^{\tan} = \mathbf{L} - \Delta t\frac{\theta}{\Pi}\frac{\partial\dot{\bar{\varepsilon}}^p}{\partial\bar{\sigma}}\mathbf{Y}\mathbf{Y}. \tag{A25}$$

The quantities of relation (A24) are evaluated at time t. Relation (A24) is substituted into the principle of virtual work.

To enforce equilibrium at the end of the time step, $t+\Delta t$, the principle of virtual work is written in the reference configuration, viz.

$$\int_V \mathbf{n}^{t+\Delta t}:\delta\mathbf{F}\,\mathrm{d}V = \int_S \mathbf{t}^{t+\Delta t}\cdot\delta\mathbf{u}\,\mathrm{d}S. \tag{A26}$$

Here, V is the reference volume and S is the part of its boundary over which tractions are imposed. $\mathbf{t} = \mathbf{N}\cdot\mathbf{n}$ is the nominal traction vector ($\mathbf{N}$ is the outward unit normal to the reference volume boundary), $\mathbf{n} = \mathbf{F}^{-1}\cdot\boldsymbol{\tau} = \mathbf{S}\cdot\mathbf{F}^T$ is the nominal stress and $\delta\mathbf{u}$ is an admissible variational displacement field that is compatible with the variational deformation gradient field, $\delta\mathbf{F}$. The explicit difference relation $\mathbf{n}^{t+\Delta t} = \mathbf{n}^t + \dot{\mathbf{n}}^t\Delta t$ as well as

$$\mathbf{n}^t:\delta\mathbf{F} = \mathbf{S}^t:\delta\mathbf{E}, \qquad \delta\mathbf{E} = \mathrm{sym}\{(\mathbf{F}^t)^T\cdot\delta\mathbf{F}\}, \tag{A27a}$$

$$\dot{\mathbf{n}}^t:\delta\mathbf{F} = \dot{\mathbf{S}}^t:\delta\mathbf{E} + \{\mathbf{S}^t\cdot(\dot{\mathbf{F}}^t)^T\}:\delta\mathbf{F}, \tag{A27b}$$

is substituted into (A26) to obtain

$$\int_V [\delta\mathbf{E}:\mathbf{L}^{\tan}:\dot{\mathbf{E}}^t + \{\mathbf{S}^t\cdot(\dot{\mathbf{F}}^t)^T\}:\delta\mathbf{F}]\,\mathrm{d}V = \int_V \left\{\frac{\dot{\bar{\varepsilon}}_t^p}{\bar{\Pi}^t}\mathbf{Y}^t - \frac{1}{\Delta t}\mathbf{S}^t\right\}:\delta\mathbf{E}\,\mathrm{d}V + \frac{1}{\Delta t}\int_S \mathbf{t}^{t+\Delta t}\cdot\delta u\,\mathrm{d}S. \tag{A28}$$

Then the usual finite element interpolation and gradient operators are introduced to obtain a linear system of equations. After applying the appropriate rate boundary conditions and solving the resulting linear system of equations, the state at time t is updated to time $t+\Delta t$. The spatial discretization is accomplished by using quadrilateral elements which are made up of four cross triangles.

Mesh

The accurate examination of the problem shown in Fig. 1, for the whole range of the applied load was accomplished with the use of meshes with various h/b_0 ratios, where b_0 is the initial notch opening. Calculations were performed for h/b_0 equal to 1400, 600, 200 and 40. Also R/h

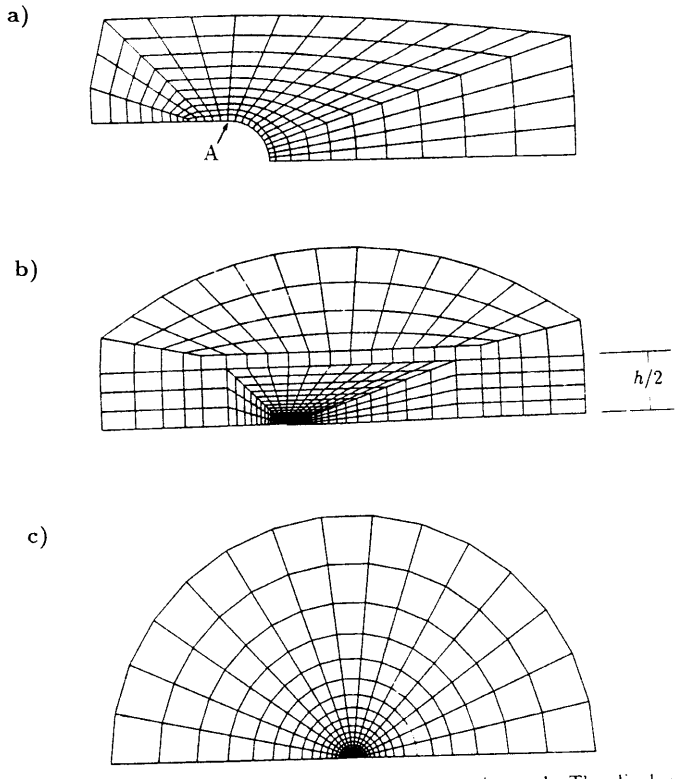

FIG. 10. Mesh used in the finite element calculations. (a) Near-tip mesh. The displacement of point A along the X_2-axis is half the crack tip opening displacement. (b) The strip represents half of the metal foil. (c) Far-field mesh. The elastic K_I-field is applied along the outer circular boundary.

was taken equal to 160 and 500. R is the radius where the elastic K-field is applied. Figure 10 shows the kind of mesh used in these calculations. Although our finite element calculations were done for different notch sizes compared to the layer thickness, the results are valid for the problem of a sharp crack, when the notch opening equals three to four times its initial value. This approach is in agreement with the finite element calculations of MCMEEKING (1977), who modeled the blunting of an initially sharp crack using a notch. It was also justified by our calculations since the final results of one geometry were the same as the initial results of the subsequent geometry. For example the distribution of the field quantities at the end of the calculations for $h/b_0 = 1400$ were coincident with those calculated at the beginning for $h/b_0 = 600$. The comparison was done after substantial blunting of the notches and for the same value of $K_I/(\sigma_0\sqrt{h})$.

APPENDIX B

Maximum mean stress and plastic zone size

Analytic estimates of the maximum mean stress and the plastic zone size, when it satisfies the relation $r_p \gg h$, have been derived. The derivation is elementary, when the characteristics of the distribution of the field quantities, observed in the finite element solution, are taken into account. The uniform through the layer thickness distribution of the field quantities at distances $r \gg h$ due to the very gradual variation of the K-field with respect to h simplifies the problem.

We may simply consider the deformation of a thin ductile layer of infinite length, bounded by infinite elastic materials, on both sides. The layer material has yield strength σ_0, Young's modulus E and Poisson's ratio ν. The elastic substrates have Young's modulus E_s and Poisson's ratio ν_s. Superscript or subscript s denotes quantities of the substrates. No subscript or superscript is used for the layer quantities. Plane strain conditions are considered. Taking into account that σ_{11} is equal to σ_{22} and σ_{12} vanishes at the crack ligament in the homogeneous material mode I K-field, we impose the following conditions for the stresses in the substrates

$$\sigma^s_{11} = \sigma^s_{22} = \sigma, \qquad \sigma^s_{12} = 0. \tag{B1}$$

σ^s_{33} is derived from the plane strain conditions. The continuity of the tractions and the displacements across the interfaces together with the uniform distribution of the field quantities in the layer leads to the following relations, valid in the layer

$$\sigma_{22} = \sigma, \qquad \sigma_{12} = 0, \qquad \varepsilon_{11} = \varepsilon^s_{11}. \tag{B2}$$

The mean stress in the layer before yielding is given by

$$\sigma_m = \frac{1}{3(1-\nu)}\left[(1+\nu) + \frac{E}{E_s}(1-\nu_s-2\nu_s^2)\right]\sigma. \tag{B3}$$

The layer mean stress increases with the ratio E/E_s. The same trend was also observed for the maximum mean stress in the actual problem, with important consequences in the opening of the crack and the cavitation phenomenon. Taking into account that the maximum mean stress, σ^*_m, develops at a distance 1–$3h$ from the crack tip in a region of plastic strains of the order of the elastic strains, we may drive an estimate of $K_I/(\sigma^*_m\sqrt{h})$ by simply setting $\sigma = K_I/\sqrt{(2\pi h)}$

$$\frac{K_I}{\sigma^*_m\sqrt{h}} = \frac{3(1-\nu)\sqrt{(2\pi)}}{1+\nu+(E/E_s)(1-\nu_s-2\nu_s^2)}. \tag{B4}$$

Relation (B4) is in very good agreement with finite element solution (see Table 2). Therefore it can be used for an estimation of the critical value of K_I, which triggers cavitation.

The layer yields when the effective stress becomes equal to σ_0. An approximate relation for the plastic zone size of the actual problem can be obtained when σ is set equal to $K_I/\sqrt{(2\pi r_p)}$

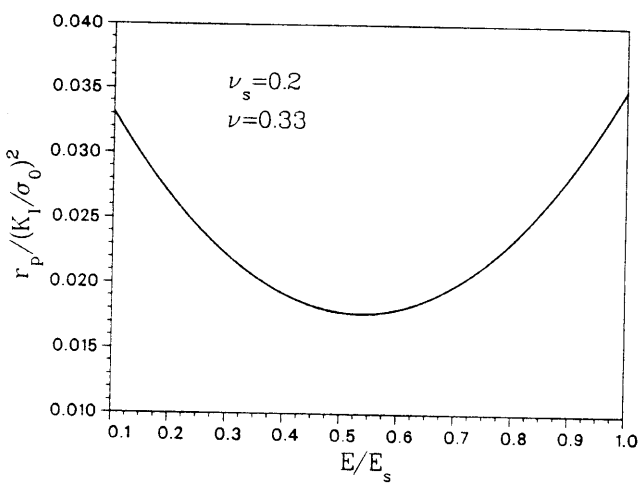

FIG. 11. Variation of $r_p/(K_I/\sigma_0)^2$ vs E/E_s, when $r_p \gg h$. The proportionality constant shows a minimum for a value of E/E_s, which is a function of the Poisson ratios of the materials.

$$r_p = \frac{(A^2 + B^2 + C^2)}{4\pi}\left(\frac{K_I}{\sigma_0}\right)^2, \tag{B5}$$

where

$$A = \frac{1}{(1-\nu^2)}\left[(1-\nu-2\nu^2) - \frac{E}{E_s}(1-\nu_s-2\nu_s^2)\right], \tag{B6a}$$

$$B = \frac{1}{(1-\nu^2)}\left[(1-\nu-2\nu^2) - \frac{E}{E_s}\nu(1-\nu_s-2\nu_s^2)\right], \tag{B6b}$$

$$C = \frac{1}{(1+\nu)}\frac{E}{E_s}(1-\nu_s-2\nu_s^2). \tag{B6c}$$

The variation of $r_p/(K_I/\sigma_0)^2$ with E/E_s is shown in Fig. 11, for $\nu_s = 0.2$ and $\nu = 0.33$. The plastic zone increases with a minimum rate when $E/E_s = 0.54$. Relation (B5) is compared with finite element solution in Table 3.